

Carboranethiol-Protected Propeller-Shaped Photoresponsive Silver Nanomolecule

Arijit Jana, Parvathy M. Unnikrishnan, Ajay K. Poonia, Jayoti Roy, Madhuri Jash, Ganesan Paramasivam, Jan Machacek, Kumaran Nair Valsala Devi Adarsh,* Tomas Base,* and Thalappil Pradeep*



Cite This: *Inorg. Chem.* 2022, 61, 8593–8603



Read Online

ACCESS |



Metrics & More

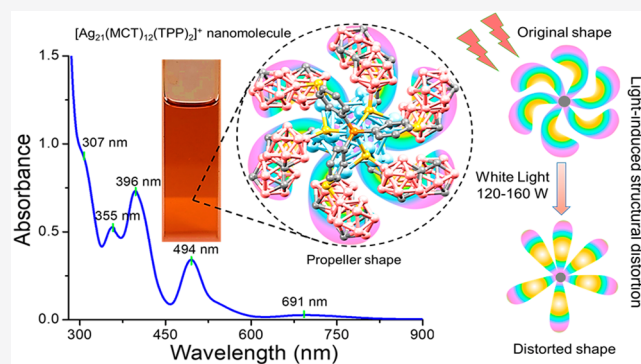


Article Recommendations



Supporting Information

ABSTRACT: We report the synthesis, structural characterization, and photophysical properties of a propeller-shaped Ag_{21} nanomolecule with six rotary arms, protected with *m*-carborane-9-thiol (MCT) and triphenylphosphine (TPP) ligands. Structural analysis reveals that the nanomolecule has an Ag_{13} central icosahedral core with six directly connected silver atoms and two more silver atoms connected through three Ag–S–Ag bridging motifs. While 12 MCT ligands protect the core through metal–thiolate bonds in a 3–6–3-layered fashion, two TPP ligands solely protect the two bridging silver atoms. Interestingly, the rotational orientation of a silver sulfide staple motif is opposite to the orientation of carborane ligands, resembling the existence of a bidirectional rotational orientation in the nanomolecule. Careful analysis reveals that the orientation of carborane ligands on the cluster's surface resembles an assembly of double rotors. The zero circular dichroism signal indicates its achiral nature in solution. There are multiple absorption peaks in its UV–vis absorption spectrum, characteristic of a quantized electronic structure. The spectrum appears as a fingerprint for the cluster. High-resolution electrospray ionization mass spectrometry proves the structure and composition of the nanocluster in solution, and systematic fragmentation of the molecular ion starts with the loss of surface-bound ligands with increasing collision energy. Its multiple optical absorption features are in good agreement with the theoretically calculated spectrum. The cluster shows a narrow near-IR emission at 814 nm. The Ag_{21} nanomolecule is thermally stable at ambient conditions up to 100 °C. However, white-light illumination (lamp power = 120–160 W) shows photosensitivity, and this induces structural distortion, as confirmed by changes in the Raman and electronic absorption spectra. Femtosecond and nanosecond transient absorption studies reveal an exceptionally stable excited state having a lifetime of $3.26 \pm 0.02 \mu\text{s}$ for the carriers, spread over a broad wavelength region of 520–650 nm. The formation of core-centered long-lived carriers in the excited state is responsible for the observed light-activated structural distortion.



INTRODUCTION

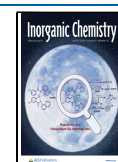
Atomically defined silver nanomolecules or nanoclusters with their core dimension below 3 nm, falling within the gap between atoms and nanoparticles, are a new class of nanomaterials with functional properties.^{1,2} Ligands on the surface of these nanoclusters have a profound role in controlling their nuclearity, shape, size, and stability. Organic ligands such as thiols,³ pyreneimethiols,⁴ phosphines,⁵ calixarenes,⁶ alkynes,⁷ carboxylic acids,⁸ deoxyribonucleic acids (DNAs),⁹ and organometallic ligands such as polyoxometalates^{10,11} have been used for the synthesis of silver nanoclusters. The size confinement, closely packed electronic energy levels, and associated electronic nature lead to numerous applications in the fields of electroluminescence,¹² sensors,¹³ catalysis,¹⁴ bioimaging,¹⁵ etc. Understanding the properties of nanoclusters depends on the determination of their atomic structures through single-crystal X-ray diffraction (SC-XRD) analysis. A handful of silver nanoclusters, including

Ag_6 ,¹⁶ Ag_{14} ,¹⁷ Ag_{22} ,¹⁸ Ag_{25} ,¹⁹ Ag_{29} ,²⁰ Ag_{44} ,²¹ Ag_{146} ,²² and several others,^{23,24} with various ligands and charge states have been characterized structurally. Obviously, for a better understanding of these nanomolecules, both structurally and electronically, and to explore their potential toward applications, it is necessary to synthesize new silver nanoclusters and study their atom-specific functional properties.

Properties of the nanoclusters, such as optical absorption, photoluminescence (PL), chirality, and circularly polarized luminescence, depend on the atomic arrangements of the core and the chemical environments of the surface ligands.^{25–28}

Received: January 22, 2022

Published: May 27, 2022



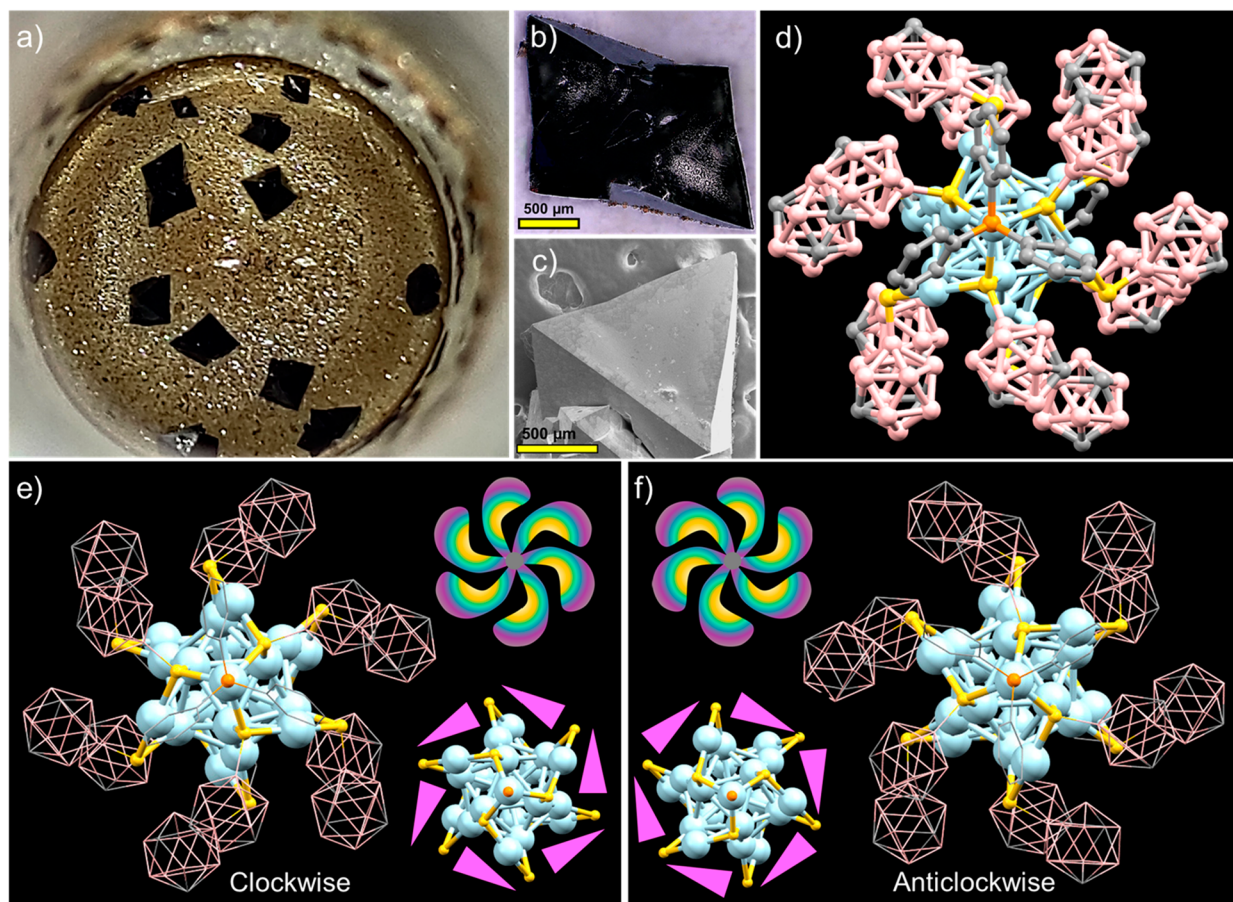


Figure 1. (a) Photograph of the bottom of the crystallization vial showing the growth of black pyramidal Ag_{21} crystals. (b) Optical microscopy and (c) FESEM images of a millimeter-sized single crystal. (d) Total structure of $[\text{Ag}_{21}(\text{MCT})_{12}(\text{TPP})_2]$ showing a propeller shape having six rotary arms along one direction. (e) View of the propeller having a clockwise rotational orientation from one side. (f) View of the same propeller with an anticlockwise rotational orientation from the other side. The top insets show schematic representations of the respective propellers, and the bottom insets show antiorientations of the respective silver sulfide core structures. Atomic color code: light blue, silver; yellow, sulfur; orange, phosphorus; pink, boron; gray, carbon. Hydrogen atoms have been removed for clarity.

Atomic arrangements in the metallic cores often determine the electronic structure. Previous studies show different types of inner-core architectures derived from pyramid,²⁹ cuboctahedron,³⁰ icosahedron,³¹ and decahedron³² with variable optical absorption features. Nanoclusters of lower atomicity (<200) are molecular in nature and exhibit multiple peaks in their respective absorption spectra, whereas an atomicity greater than 200 gives particles with plasmonic absorption features.^{33–35} Not only the atomic structure but also the nearest chemical environments, such as the outer shell of the ligands,³⁶ temperature,³⁷ pressure,³⁸ solvents,³⁹ and coordinating ions,⁴⁰ have a profound effect on their absorption as well as emission properties.

The reactivity is a major concern for many silver nanoclusters. Recently, we showed light-activated conversion of the Ag_{42} nanocluster.⁴¹ Another report showed that a bare Ag_{17}^+ nanocluster reacts with carbon monoxide⁴² and acetylene gases and forms different adduct species.⁴³ Ligand-exchange-induced structural conversion was also noticed for a few silver nanoclusters.⁴⁴ Atomic exchange between two nanoclusters in solution leads to a mixture of alloy nanoclusters through the formation of transient dimer species, following a concerted reaction pathway.^{45,46} The use of a suitable surface ligand determines the stability of the nanoclusters. Among

different thiols, carboranethiols are gaining prominence because of their extraordinary thermal stability, robust 3D structure, and specific borane aromaticity with electron delocalization all over the icosahedral boron–carbon framework.⁴⁷ Recently, Zang et al. have synthesized carboranethiol-protected silver nanoclusters and nanocluster-assembled frameworks such as Ag_{14} ,⁴⁸ Ag_{17} ,⁴⁹ and Ag_{30} .⁵⁰ Among such clusters, *o*-carboranealkynyl-protected Ag_{14} and Cu_6Ag_8 nanoclusters behave as efficient hypergolic materials, which ignite spontaneously upon their exposure to an oxidizer.⁵¹

RESULTS AND DISCUSSION

In this work, we present the synthesis of a *m*-carborane-9-thiol (MCT)- and triphenylphosphine (TPP)-coprotected silver nanocluster of the formula $[\text{Ag}_{21}(\text{MCT})_{12}(\text{TPP})_2]^+$ (abbreviated as Ag_{21}) using ligand-exchange-induced structure transformation (LEIST) of $[\text{Ag}_{18}(\text{TPP})_{10}\text{H}_{16}]^{2+}$ (abbreviated as Ag_{18}). Details of the synthesis and characterization of Ag_{18} through UV–vis absorption and mass spectrometry studies are presented in Figure S1. During the synthesis of Ag_{21} through the LEIST reaction, 10 mg of purified Ag_{18} dissolved in methanol was reacted with 8 mg of the MCT ligand. After 2 h of exchange reaction, the initially green Ag_{18} solution gradually turned red, characteristic of Ag_{21} , through yellowish and

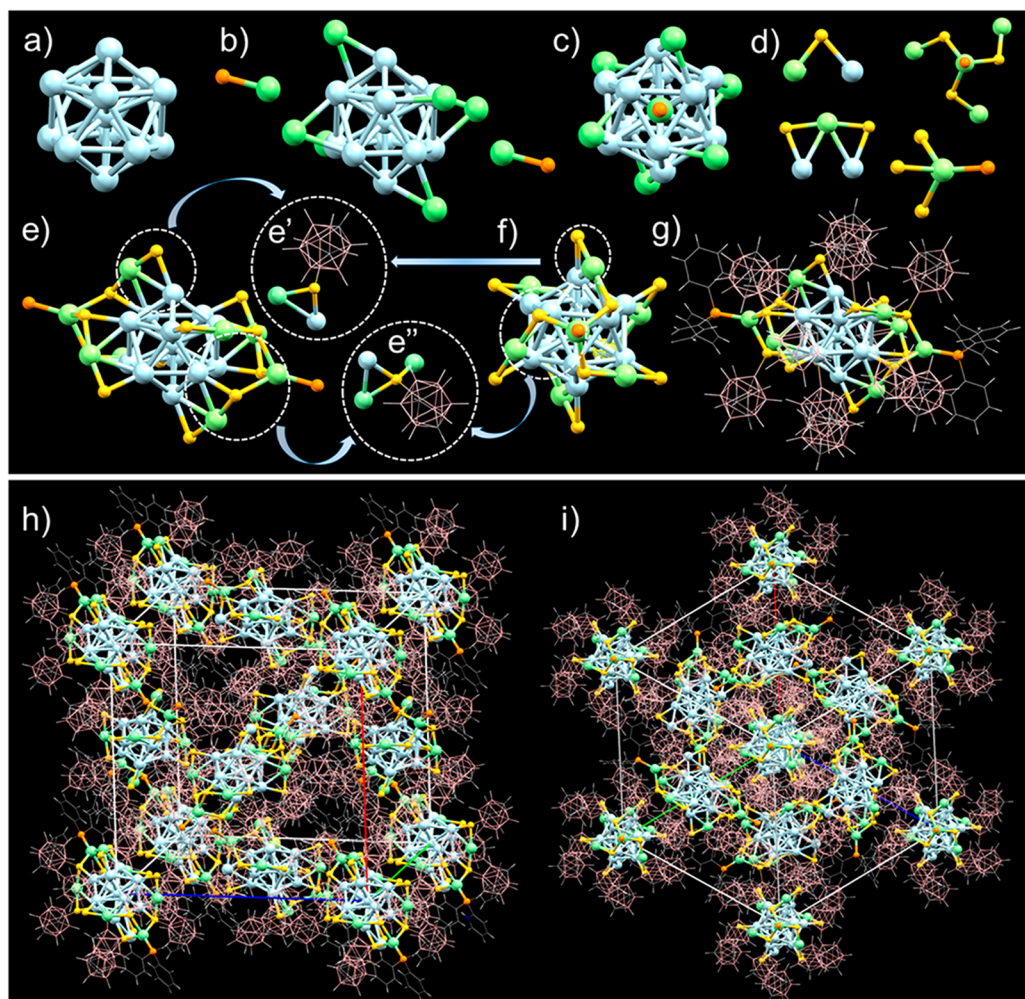


Figure 2. Structural anatomy of the Ag_{21} nanocluster: (a) central icosahedral Ag_{13} core; (b and c) $\text{Ag}_{13}\text{-Ag}_6\text{-Ag}_2\text{P}_2$ -layered structure viewed from two different orientations; (d) different types of Ag-S motifs present in the cluster; (e and f) a silver sulfide skeleton structure without MCT and Ph ligands; (e' and e'') different types of carborane binding; (g) complete structure of $[\text{Ag}_{21}(\text{MCT})_{12}(\text{TPP})_2]^+$ having MCT and TPP ligands; (h) face-centered-cubic unit cell molecular packing of the nanocluster viewed along the axial directions; (i) MOF-like packing viewed from a corner of the cube. Color code: light blue, inner core Ag; green, outer core Ag; yellow, sulfur; orange, phosphorus; pink, boron; gray, carbon; white, hydrogen.

brownish intermediate nanoclusters. Figure S2 shows the photographs of this color change. Time-dependent UV-vis absorption spectra (shown in Figure S3) measured during the reaction showed that the formation of Ag_{21} started after 30 min of an exchange reaction. Overnight size focusing in methanol led to the formation of monodispersed nanoclusters having sharp absorption features. Each aspect of compositional, structural, and charge-state characterization of $[\text{Ag}_{21}(\text{MCT})_{12}(\text{TPP})_2]^+$ is presented consequently.

For diffraction analysis, suitable single crystals were obtained after 7 days of slow diffusion of hexane vapors into a concentrated nanocluster solution in dichloromethane (DCM; 30 mg/mL) at $\sim 4^\circ\text{C}$. Although the nanocluster is dark red in its DCM solution, millimeter-sized pyramidal black crystals formed upon crystallization. A photographic image of the as-grown crystals is shown in Figure 1a. The optical microscopy images shown in Figures 1b and S4 depict the pyramidal surfaces of the crystals, which were further verified by field-emission scanning electron microscopy (FESEM) images, as shown in Figures 1c and S5a,b. The energy-dispersive spectroscopy (EDS) spectrum and respective elemental

mapping (Figures S5c and S6) fit the nominal stoichiometry of the cluster, confirming the presence of boron, carbon, sulfur, phosphorus, and silver in the crystals. The as-grown crystals show well-defined diffraction spots (Figure S7) under the X-ray beam, which is indicative of good crystallinity. The powder X-ray diffraction (PXRD) patterns of the microcrystalline samples are in good agreement with the diffractogram generated from the SC-XRD data (Figure S8a). SC-XRD reveals that the nanocluster crystallizes in a cubic crystal system with the $Pa\bar{3}$ space group and a cell volume of 19130 \AA^3 .

Further details of the structural parameters are summarized in Tables S1 and S2. The complete molecular structure of the nanomolecule including its ligand shell, as shown in Figure 1d, resembles a propeller with six rotary arms, where the TPP centers represent the nodes. Although the nanomolecule does not have a 6-fold symmetry axis, the spatial orientation of the carborane ligands resembles a propeller in 2D projection. Careful analysis reveals that Ag_{21} looks like a left-handed propeller when viewed from a TPP at the head, while it is right-handed when viewed from the opposite direction (Figure

1e,f). The orientation of the silver sulfide structure is also opposite to that of the orientation of carboranes, similar to the bidirectional orientation in the nanomolecule. The inherent chirality of the cluster, as observed in its single crystal, was investigated using circular dichroism (CD) measurements. However, the CD spectrum shown in Figure S9 shows no chiral response in the wavelength range of 240–800 nm, suggesting an achiral nature of the cluster in the DCM solution. The symmetric character of the nanomolecule in solution is perhaps due to the dynamic nature of carborane ligands on the cluster surface. Another reason behind the lack of a CD signal is the intense absorption features of the nanomolecule in comparison to the local orientations of the pendant groups. Further analysis reveals the presence of a C_3 rotational symmetry axis along the TPP node of the nanomolecule, and the orientation of carborane ligands on its surface looks like an assembly of double rotors (as shown in Figure S10).

Another independent view of the nanomolecule gives an oval-like shape with two TPP units at the head and tail positions of the cluster (Figure S11). The ORTEP image in Figure S12 shows the cluster's oval-like shape with specific packing of the ligands. The distance between the two phosphorus atoms at antipodal positions of the cluster is 17.139 Å. A total of 12 carborane ligands enclose the surface of the cluster through silver–thiolate bonds. The arrangement of the carboranes is in a 3:6:3 fashion on the outer surface of the cluster along the P–P axis (as shown in Figure S13). The three MCT ligands near the head are in a staggered conformation with three other MCT ligands near the tail (as shown in Figure S14). The staggered orientation of these carboranes determines the opposite orientation of the propeller.

The structural anatomy of Ag_{21} reveals a central icosahedral Ag_{13} core and a shell of eight silver atoms (Figure 2a–c). The average Ag–Ag bond distance in the Ag_{13} core is 2.795 Å, suggesting strong metallic bonding. Six out of the remaining eight silver atoms are directly connected to the Ag_{13} core through Ag–Ag bonds with a distance range of 2.924–3.076 Å, showing weaker Ag–Ag bonding compared to that in the core. The remaining two silver atoms are 4.305 Å away from the nearest Ag_3 triangular facets and 6.168 Å from the central silver atom. These two silver atoms are connected with the cluster through three Ag–S–Ag bonds in a tripod fashion with an average Ag–S bond distance of 2.637 Å. Detailed analysis reveals that the 12 carboranes bind with the outer surface through different types of silver sulfide motifs (Figure 2d–f). Among them, six carboranes present on the body of the cluster are connected by six Ag_2S motifs, where each sulfur is bridged between one silver atom from the Ag_{13} core with an Ag–S bond distance of 2.527 Å and one silver from the outer shell with an Ag–S distance of 2.378 Å (Figure 2e'). The remaining six carboranes near the TPPs are connected by Ag_3S motifs, where one silver is isolated and the other two are from the $Ag_{13}@Ag_6$ unit (Figure 2e''). A comparison between $[Ag_{25}(SR)_{18}]^-$ and $[Ag_{21}(MCT)_{12}(TPP)_2]^+$ (as shown in Figures S15 and S16) shows that both of them have central Ag_{13} icosahedra.¹⁹ However, the remaining 12 silver atoms of $[Ag_{25}(SR)_{18}]^-$ capped the triangular icosahedral facets through μ_3 and μ_2 capping modes with average bond distances of 2.858–3.189 Å, whereas in our Ag_{21} , only six silver atoms capped the triangular facets through μ_2 capping mode with average bond distances of 2.924–3.076 Å. Fewer atoms capping the central Ag_{13} icosahedron in Ag_{21} in comparison to

Ag_{25} and also binding of the additional two silver atoms in Ag_{21} not being directly connected to the silver core can be attributed to the greater steric requirements of the bulky carborane ligands. There are other reports of the Ag_{21} nanocluster, protected by dithiophosphate⁵² and diselenophosphate⁵³ ligands with a central icosahedral Ag_{13} core connected with eight μ_3 -capped silver atoms. Yet another perspective is that the bulkiness of the ligand has a proven effect on the structure of the metal part of the cluster, which could be potentially further investigated using narrower 10-vertex carboranes, dicarba-*closo*-decaboranes.

The molecular packing of the nanomolecule in the single crystal shown in Figure 2h presents a face-centered-cubic-type arrangement with eight clusters positioned in the corners of the cube, having an intercluster distance of 26.745 Å and the remaining six clusters centered on the faces of the cube. The packing density is $4 [(8 \times \frac{1}{8}) + (6 \times \frac{1}{2})]$ in the unit cell. Extended packing showed (Figure S17) A–B–A–B-type lamellar packing with oval shapes of the clusters along each (*a*, *b*, and *c*) axis. A view of the packing (as shown in Figures 2i and S18 and S19) through the corners of the cube showed a metal–organic framework (MOF)-like structure. Careful analysis reveals that a view of the intercluster packing through the corner of the cube shows that eight clusters have propeller orientations, whereas the remaining six clusters have oval shapes (Figure S19). Views along *a*, *b*, and *c* corners lead to two clusters each having propeller orientations, whereas the remaining 12 clusters have oval shapes (Figure S18). Multiple intercluster BH–BH and BH–CH van der Waals interactions among the carboranes are the reason behind their molecular packing (as shown in Figure S20). A recent study of double-helical DNA-like intercluster packing shows engineering design aspects of the metallic nanocluster.⁵⁴ In this direction, the propeller-like structure and MOF-like packing arrangements make the Ag_{21} nanomolecule interesting.

The UV–vis absorption spectrum of Ag_{21} (as shown in Figure 3a) in its DCM solution is characteristic and has bands at 691, 494, 396, 355, and 307 nm, which are typical for a confined electronic structure. Time-dependent absorption spectra showed the stability of the crystals up to 60 days (Figure S21) under ambient conditions. 3D carboranes present on the surface of the cluster may be the reason behind their

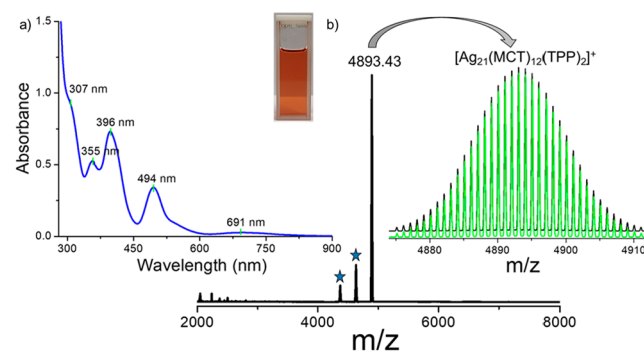


Figure 3. (a) UV–vis absorption spectrum of Ag_{21} in DCM (inset: photographic image of the cluster in DCM). (b) Full-range high-resolution ESI-MS spectrum of the cluster having a peak at m/z 4893.43 in a monopositive charge state, assigned as $[Ag_{21}(MCT)_{12}(TPP)_2]^+$ [right inset: exact matching of the experimental spectrum (black) with the theoretical spectrum (green)]. Each ★ indicates TPP loss from the parent peak.

superior stability. The absorption spectra of Ag_{21} in different solvents such as 1,2-dichlorobenzene, acetone, chloroform, DCM, methanol, ethanol, dimethylformamide (DMF), and dimethyl sulfoxide (DMSO) were measured (as shown in Figure S22). All of the spectra were identical except in DMF and DMSO. Broadening of the spectral bands, along with small shifts in their peak positions, indicate solvatochromism. The ligand-centered ground-state orbitals may be prone to interaction with these polar aprotic solvents, and this could explain the spectral broadening.

The molecular composition of Ag_{21} in solution was studied using high-resolution electrospray ionization mass spectrometry (ESI-MS). The sample preparation and instrumental conditions are specified in the Supporting Information. The full-range high-resolution ESI-MS spectrum shown in Figure 3b gave a major peak centered at m/z 4893.43 in positive-ion mode. An expanded view of the peak shows a characteristic peak-to-peak separation of m/z 1, which confirms the charge state as $1+$. The peak was assigned to $[\text{Ag}_{21}(\text{MCT})_{12}(\text{TPP})_2]^+$. The isotopic distribution of the experimental spectrum matches that of the theoretical spectrum. Two other fragment peaks at m/z 4630.5 and 4368.35 are assigned to the sequential mass loss of 262 amu, suggesting two TPP losses from the parent nanocluster. The cluster did not show features in the negative-ion mode. However, the characteristic ion peak at m/z 61.98 in negative-ion mode confirms the presence of NO_3^- as a counterion in the crystal (Figure S23).

We analyzed the free electron count of $[\text{Ag}_{21}(\text{MCT})_{12}(\text{TPP})_2]^+$ to investigate its stability. For this nanomolecule, 21 silver atoms have one valence ($5s^1$) electron each. Therefore, the total metal electron count is $N_{\text{VA}} = 21$. The 12 MCT ligands are electron-withdrawing, whereas the TPP ligands are neutral and so ligand electrons are involved in the binding, where $M = 12$. The cluster has a net charge of $1+$, so that $Z = 1$. This gives a valence electron count of $8e$ ($N_{\text{VA}} - M - Z = 21 - 12 - 1 = 8$), indicating a superatomic electronic configuration.^{55,56} This $8e$ superatomic cluster having a closed-shell electron distribution in $1s^21p^6$ superatomic orbitals is the reason behind its electronic stability.

In order to gain additional insight into bonding and structure, we studied the MS/MS fragmentation of the molecular ion peak (Figure 4). Fragmentation studies were carried out by varying the collision energy (CE) by selecting the parent ion peak at m/z 4893.43 with a charge state of $1+$. A sequential increase of CE from 2 to 20 (in instrumental units) resulted in two consecutive mass losses of 262 units, which correspond to two TPP fragments. The loss of TPP fragments at low CE is due to a weak Ag–P bond, having a bond length of 2.401 Å. At a CE of 25, the peak at m/z 4368.25 displayed the loss of both TPPs. A further increase of the CE up to 70 led to no more fragmentation of the peak at m/z 4368.25, revealing strong bonding of the carboranes within the cluster. At a CE of 75, new fragments are observed from m/z 4368.25, careful analysis of which reveals a sequential mass loss of 283 units (Figure S24). The m/z 283 mass loss fits the combined mass of one silver atom and one MCT ligand. So, this sequential loss is due to the systematic loss of Ag–MCT. A further increase of the CE up to 150 shows eight sequential losses of Ag–MCT fragments. Another series of mass fragments with the mass loss of MCT units (m/z 175) was also present. The strong appearance of Ag–MCT loss peaks in comparison to MCT loss peaks indicate strong B–S bonds, which is different from the *o*-carborane-1,2-dithiol-protected Ag_{42}

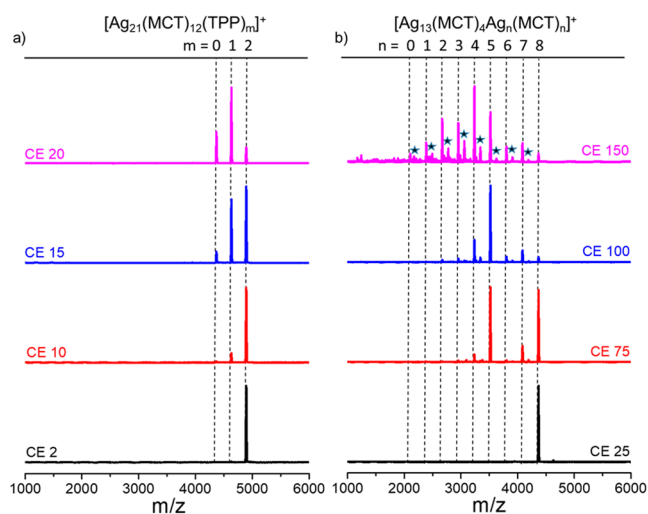


Figure 4. CE-dependent MS/MS pattern of the parent cluster (a) up to a CE of 20, showing only two TPP losses, and (b) a further increase in the CE up to 150, leading to eight Ag–MCT losses. Each ★ peak shows the sequential loss of MCT alone.

nanocluster.⁴¹ To understand the stability of the fragmented peaks, we calculated the valence electrons of each fragmented clusters (Table S3).

The Ag–MCT loss peaks have eight valence electrons in comparison to nine valence electrons of fragments generated due to MCT losses. The closed-shell magic electronic configuration makes Ag–MCT fragments more stable than MCT loss fragments. This systematic fragmentation correlates very well with the structure of the nanocluster with eight silver atoms outside the Ag_{13} core. The CE-dependent fragmentation experiments correlate with the structural complexity and nature of bonding of the nanomolecule.

The size of Ag_{21} was characterized using transmission electron microscopy (TEM). TEM images (as shown in Figure S25) showed particles with an average diameter of 1.91 ± 0.2 nm. The EDS elemental mapping confirms the elemental composition of the clusters consisting of silver, sulfur, phosphorus, carbon, and boron in the clusters. The atomic ratio of silver and sulfur is 1.47, which nearly correlates to the ratio of 21:12 (1.75). The presence of all of the elements has been further confirmed using X-ray photoelectron spectroscopy (XPS). XPS spectra (Figure S26) have signature features of the respective elements. The binding energies of 368.3 and 374.3 eV for Ag $3d_{5/2}$ and $3d_{3/2}$ are due to silver(0). A single peak at 189.8 eV for the B 1s region is characteristic of boron in carborane moieties, whereas three peaks at 283.6, 285.1, and 286.9 eV in the C 1s region of the spectra indicate different types of carbon atoms originating from carborane as well as TPP ligands. The peak at 131.4 eV is due to P 2p of TPP ligands. Along with other characteristic peaks, two peaks at 406.7 and 531.6 eV are due to N and O 1s, respectively, which exhibit the presence of nitrate ions in the crystals.

Multinuclear NMR spectra of a free MCT ligand and Ag_{21} were recorded to confirm the binding of the ligands. Free MCT ligands display characteristic sharp ^{11}B NMR signals at -3.2 , -6.8 , -9.8 , -13.5 , -14.8 , -18.5 , and -21.7 ppm with an integration ratio of 1:2:1:2:2:1:1, respectively, for 10 boron atoms (Figures S27 and S28 and Table S4). Around 30 mg of purified clusters dissolved in 0.75 mL of CDCl_3 was used to measure the NMR spectrum of Ag_{21} . The ^{11}B NMR spectrum

in Figure S29 shows a set of seven sharp peaks at +2.22, +0.91, -5.40, -8.20, -12.05, -14.24, and -17.84 ppm due to the presence of a nonequivalent boron atom of 12 *m*-carborane ligands. The broadness of the peaks is due to the high electron density of the metallic silver core near the carborane. The proton-decoupled ^{13}C NMR spectrum (Figure S30) showed the signature peaks of the carbon atom for carborane at 54.32 and 55.53 ppm. Along with the carborane peaks, a set of peaks in the region of 128.48–133.93 ppm appear because of the aromatic carbons of TPP ligands. A broad ^{31}P NMR peak (as shown in Figure S31) at 8.67 ppm shows the binding of TPP. It may be noted that free TPP exhibits a sharp feature at -5.66 ppm. Furthermore, to explore the binding of the ligands, we measured the IR spectrum of the Ag_{21} crystals and compared it with that of the free MCT ligand (Figure S32). The appearance of similar vibrational peaks proves the presence of carboranes in the cluster. Along with the carborane features, we observed three new peaks at 1385, 1435, and 1480 cm^{-1} , which are due to the antisymmetric N–O stretching of NO_3^- ions present in the crystal lattices.⁵⁷ Although we have not observed nitrate as a counterion in the single-crystal structure, the presence of a NO_3^- signature in the IR and ESI-MS spectrum, along with the characteristic N 1s of nitrate in XPS, confirming the positive charge of the cluster with nitrate as the counterion. We measured the Raman spectra of the clusters and compared the spectral features with those of the free MCT ligand (Figure S33 and Table S5). The assignments of the spectral features are similar to those in the literature.⁵⁸ Characteristic vibrational peaks of MCT in Ag_{21} are nearly similar to those of free MCT. The doublet peaks of C–H stretching (3051 and 3070 cm^{-1}) and B–H stretching (2618 and 2645 cm^{-1}) become singlet peaks at 3081 and 2652 cm^{-1} , respectively. Similarly, red shifts of the C–H and B–H vibrational features were observed as a result of the effect of the chemical environment in Ag_{21} . Identical vibrational features of the icosahedral cage breathing mode at 760 cm^{-1} indicate the indistinguishable chemical environment of the carborane cage. Raman studies show that the B–H and C–H chemical environments are more affected in comparison to the carborane cage.

Molecular absorption features of the nanomolecule were assigned on the basis of their comparison with the computationally simulated spectra using time-dependent density functional theory (TDDFT) calculations in a grid-based projector-augmented-wave method. To reduce the computational cost, we replaced PPh_3 as PH_3 . Linear-response TDDFT calculations were carried out to simulate the optical absorption spectra. A detailed discussion of the theoretical calculations is presented in the Supporting Information. The simulated absorption spectrum of the optimized structure in the gas phase matches well with the experimental spectrum (Figure 5a). Changes seen are also attributed to the effect of the solvents. To understand the effect of phosphines, we also optimized the structure with phosphines. The calculated absorption spectrum is almost similar to the earlier structure without phosphines (as shown in Figure S34). The values of the oscillator strength of all of these transitions are summarized in Table S6. Figures S35–S38 show the contribution of the molecular orbitals corresponding to the transition at 672, 565, 494, and 422 nm, respectively. The electronic transition at 672 nm (1.84 eV) originates as a result of the transition from HOMO–1 and HOMO–2 to LUMO and LUMO+1 (where HOMO = highest occupied molecular orbital and LUMO =

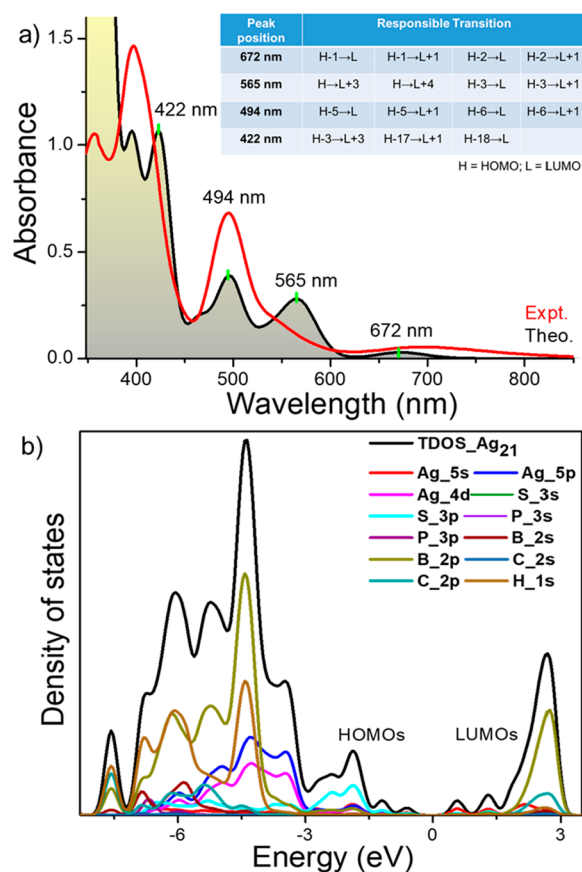


Figure 5. (a) Experimental absorption spectrum of the Ag_{21} nanocluster and correlation with the theoretical spectrum. The inset shows the molecular orbitals responsible for the features (H = HOMO and L = LUMO). (b) DOS analysis with respect to individual atomic orbitals.

lowest unoccupied molecular orbital). The electron density maps show that this peak is due to charge transfer within the metallic core. The next prominent peak at 494 nm (2.51 eV) is associated with the transition from HOMO–5 and HOMO–6 to LUMO and LUMO+1. Electron density maps show charge transfer from the delocalized HOMOs in the shell to the core-centered LUMOs.

Another prominent peak at 422 nm (2.94 eV) is associated with the transition from HOMO–3, HOMO–17, and HOMO–18 to LUMO+3, LUMO+1, and LUMO. This transition is associated with charge transfer from the ligand-shell-delocalized HOMO to the kernel-localized LUMO. For an additional assessment of the effect of hybridization on the formation of molecular orbitals, the density of states (DOS) was analyzed in the entire energy region (Figure S39). The middle of the plots was set to zero to indicate the Fermi level. Orbitals of negative energy are considered to be HOMOs, whereas orbitals with positive energy are considered to be LUMOs. Ag 5s and 5p orbitals and S 3p orbitals dominated the energy levels (i.e., HOMOs and LUMOs) near the Fermi level. The deeply occupied orbitals having energy of -1.5 eV are mostly dominated by the S 3p atomic orbitals, and deeply unoccupied orbitals having energy of >math>1.5\text{ eV}</math> are occupied by the 2p atomic orbitals of boron and carbon atoms. According to the DOS calculation, low-energy transitions are silver-core-centered, whereas higher energy transitions are mostly ligand-centered.

Furthermore, we studied the PL property of Ag_{21} in solution by dissolving a few crystals in DCM. We did not observe any emission from the solution under a 365 nm UV lamp (as shown in the inset of Figure 6). PL measurements show (Figure 6) a sharp emission centered at 814 nm in the near-IR (NIR) region. The asymmetry of the emission line shape may be contributed by the detector response in the NIR region. The sharpness of the emission spectrum exhibits their molecular nature. The sharp excitation maximum at 459 nm is near to the edge of the absorption maximum at 494 nm, which is ligand-shell-to-metal-core (LSMC) charge transfer. The apparent Stokes shift of 2053 cm^{-1} was calculated from the energy gap between the absorption edge and the emission maximum (Figure S40). Such a modest Stokes shift also indicates closely spaced energy levels of the nanocluster.

We studied the thermal and light sensitivity of the cluster. The cluster shows thermal stability up to $100\text{ }^{\circ}\text{C}$ at ambient conditions. Illumination with white light leads to structural distortion, even at room temperature ($25\text{ }^{\circ}\text{C}$). Figure 7a shows a schematic representation of the structural stability upon heating and structural distortion upon light irradiation. Photographic images (Figure 7b) of reddish microcrystalline samples showed no visible color change upon heating at $100\text{ }^{\circ}\text{C}$. To investigate the thermal stability, we measured the UV–vis and Raman spectra after heating at different temperatures. About 8–10 mg of a microcrystalline powder was used for heating (exposure time, 4 h). Identical absorption features (Figure 7d) exhibit the structural stability of the clusters after $100\text{ }^{\circ}\text{C}$ heating. Furthermore, Raman measurements (Figure 7e) showed identical spectral signatures until $100\text{ }^{\circ}\text{C}$, which further confirms the same. The sample heated at $120\text{ }^{\circ}\text{C}$ showed signatures of changes with the emergence of new features at 1346 and 1593 cm^{-1} . Thermogravimetric analysis (TGA) and differential thermogravimetric (DTG) studies (Figure 7f) showed no weight loss up to $140\text{ }^{\circ}\text{C}$. We performed a differential scanning calorimetry (DSC) study in a temperature range of -90 to $+750\text{ }^{\circ}\text{C}$. Figures S41 and S42 show the DSC data of the cluster. The linear thermogram from

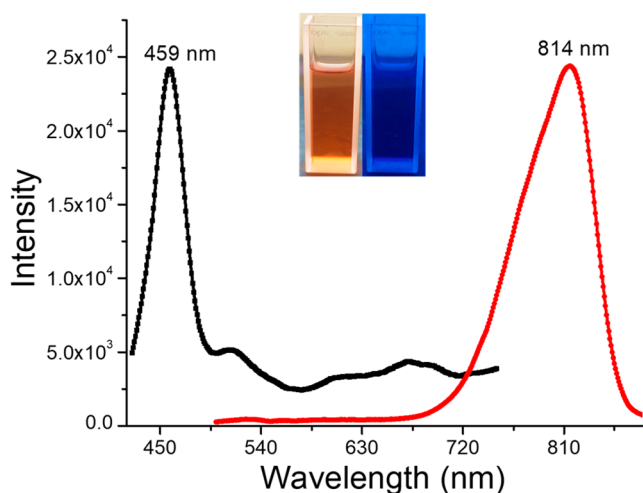


Figure 6. PL excitation (black) and emission (red) spectra of Ag_{21} were measured in its DCM solution. The emission spectrum was measured using 460 nm excitation. The excitation spectrum was measured for 814 nm emission. The inset shows optical images of the nanocluster under daylight (left) and under a 365 nm UV lamp (right).

-90 to $+125\text{ }^{\circ}\text{C}$ confirms thermal stability. An exothermic peak observed at $140\text{ }^{\circ}\text{C}$ is probably due to ligand ordering.

Interestingly, we observed spectral broadening of the UV–vis absorption features upon illumination of the microcrystalline samples using white light (xenon arc lamp). Lamp-power-dependent studies (exposure time 4 h) showed that up to $\sim 100\text{ W}$ there was no variation of the absorption features. In the range of 120 – 160 W , spectral features become broad because of the formation of distorted clusters. Beyond 160 W , even more drastic changes are seen. Spectra were measured after dissolving the irradiated samples in DCM. Raman studies of microcrystalline samples (as shown in Figure 7h) show that, up to 100 W , there was no change in the vibrational features, whereas samples exposed at 120 and 160 W had multiple new peaks. We also observed similar intensities of the BH (2652 cm^{-1}) and CH (3081 cm^{-1}) stretching vibrations after 120 and 160 W light exposure, and the intensity of the cage breathing mode (760 cm^{-1}) also reduced significantly, which implies a strain in the carborane moieties. The appearance of new peaks near 1000 – 1300 cm^{-1} (the CH and BH bending regions) also confirmed structural distortion. To explore the molecular stability, we measured ESI-MS of the samples, exposed to 120 W light. The characteristic peak at m/z 4893.43 confirms its stability. Therefore, light-illuminated changes in the crystalline state in the initial stages are attributed to possible molecular distortions in the structure, although more studies are necessary to understand the precise nature of the changes. An earlier investigation of the mechanical properties of cluster crystals using nanoindentation would suggest a flexible character for cluster crystals.⁵⁹ Upon further exposure, at 180 W and above, it appears that additional changes are happening, as suggested by the emergence of new bands, at 1346 and 1593 cm^{-1} . These bands are similar to those arising during thermal annealing, which suggests that both thermal and photochemical changes result in the same product eventually. However, more studies are necessary to confirm this.

To understand the electron dynamics responsible for the multiple absorption features and photoresponsivity, we performed femtosecond and nanosecond transient absorption (fs–ns-TA) spectroscopy. Experimental details of the measurements are given in the Supporting Information. Figure 8 shows the summarized fs–ns-TA data of Ag_{21} nanocluster, using a 400 nm , 120 fs pump laser with a fluence of $170\text{ }\mu\text{J}/\text{cm}^2$. The contour plot of the obtained result is shown in Figure 8a. To better understand the excited-state features, the spectral profile of TA at selected time delays is plotted in Figure 8b. The figure shows that TA is primarily dominated by the two types of excited-state absorption (ESA) located in the region of $\sim 465\text{ nm}$ and broad ESA beyond 500 nm . A relatively weak negative signal (photobleach) is observed near 490 nm . It is at the position of the peak observed in the optical absorption of nanocluster (Figure 3a) and arises as a result of phase space filling by pump excitation.

The weak ESA feature centered at $\sim 465\text{ nm}$ is observed to have a short lifetime ($<10\text{ ps}$) and disappear rapidly compared to the other ESA feature (Figure S43). Here, it is also noticed that photobleach growth accompanies the ESA decay. Such a behavior suggests that the ESA feature is possibly due to structural relaxation or charge transfer from the core to shell. Figure 8c shows the femtosecond-decay profiles associated with the broad ESA features. It offers a prolonged transient behavior and does not decay in the femtosecond window. To determine the kinetics of the long component, we measured

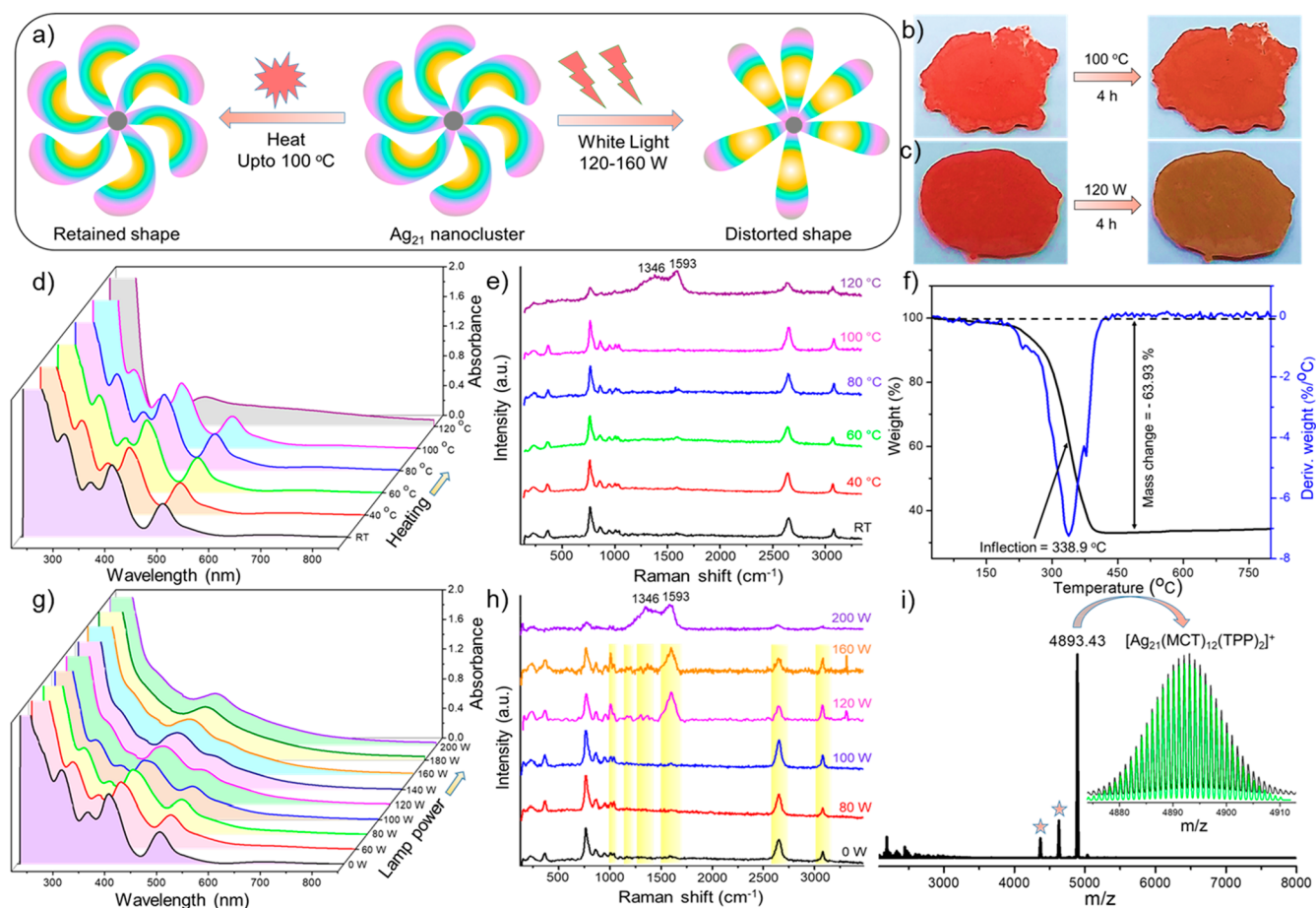


Figure 7. (a) Schematic representation showing the thermal and photo-illumination effects on Ag_{21} crystals. (b) Photographic images showing no visible color change after heating at $100\text{ }^{\circ}\text{C}$. (c) Photographic images showing a visible color change after 120 W light illumination. (d) UV–vis absorption spectra after heating at different temperatures. Identical absorption spectra were observed up to $100\text{ }^{\circ}\text{C}$. (e) Raman spectra of Ag_{21} crystals after heating at different temperatures. (f) TGA and DTG analyses showing thermal stability of the cluster up to $140\text{ }^{\circ}\text{C}$ with an inflection at $338.9\text{ }^{\circ}\text{C}$. (g) Sequential UV–vis absorption spectra after light exposure using different lamp powers (exposure time of 4 h on each time). (h) Raman spectra showing the appearance of new vibrational peaks using lamp powers of $120\text{--}160\text{ W}$. Changes are highlighted. (i) Positive-ion-mode ESI-MS spectrum showing the presence of the cluster after 120 W light exposure. The inset shows an exact matching of the experimental (black) and theoretical (green) spectra. The peaks labeled \star indicate TPP losses from the parent Ag_{21} .

ns-TA spectroscopy in Figure 8d, where it decays in the window of $30\text{ }\mu\text{s}$. The curve shown is fitted with a single-exponential function and renders a decay constant of $3.26 \pm 0.02\text{ }\mu\text{s}$. Such a long lifetime of carriers in the excited state is also observed in other gold and silver nanoclusters possibly because of ligand-to-metal charge transfer and the inherent geometry of the cluster.⁶⁰ The stable carriers predominantly center in the metallic core region of the excited state throughout the wavelength range of $520\text{--}650\text{ nm}$, which are likely to be the reason behind the photoresponsive nature.

CONCLUSION

In conclusion, we synthesized a MCT- and TPP-coprotected silver nanocluster, $[\text{Ag}_{21}(\text{MCT})_{12}(\text{TPP})_2]^+$, starting from the Ag_{18} precursor cluster, protected with TPP and hydride. SC-XRD reveals that the nanocluster has an Ag_{13} central icosahedral core, which is connected with six silver atoms through direct Ag–Ag bonds and two other silver atoms connected via three Ag–S–Ag bonds in a tripodal fashion. Twelve carboranes surround the cluster as thiolates in a layered fashion, whereas two TPPs are connected at the head and tail positions of the oval-like cluster core through Ag–P bonds.

The MCT ligands assemble into an array resembling a propeller having six rotary arms when viewed along its TPP–TPP axis. A bidirectional rotational orientation of the silver sulfide core with the MCT ligand was observed in the nanomolecule. High-resolution mass spectrometry showed the systematic loss of two TPP ligands at low CEs and eight carborane ligands with silver atoms at high CEs, confirming strong bonds between the carborane ligands and the silver cluster. DFT has helped in the understanding of the experimental electronic absorption spectrum. The cluster showed a sharp NIR emission at 814 nm . Although the Ag_{21} cluster shows an ambient thermal stability of up to $100\text{ }^{\circ}\text{C}$ in its solid state, it manifests light-triggered structural distortion, as shown in UV–vis absorption and Raman spectroscopy studies. fs–ns-TA studies proved the formation of stable excited-state carriers with a lifetime of $3.26 \pm 0.02\text{ }\mu\text{s}$ in the $520\text{--}650\text{ nm}$ region, responsible for its photoresponsivity. Altogether, these studies suggest that thermally stable and photochemically active atomically precise silver clusters of unique structure and inherent beauty can be formed using carboranethiols as ligands.

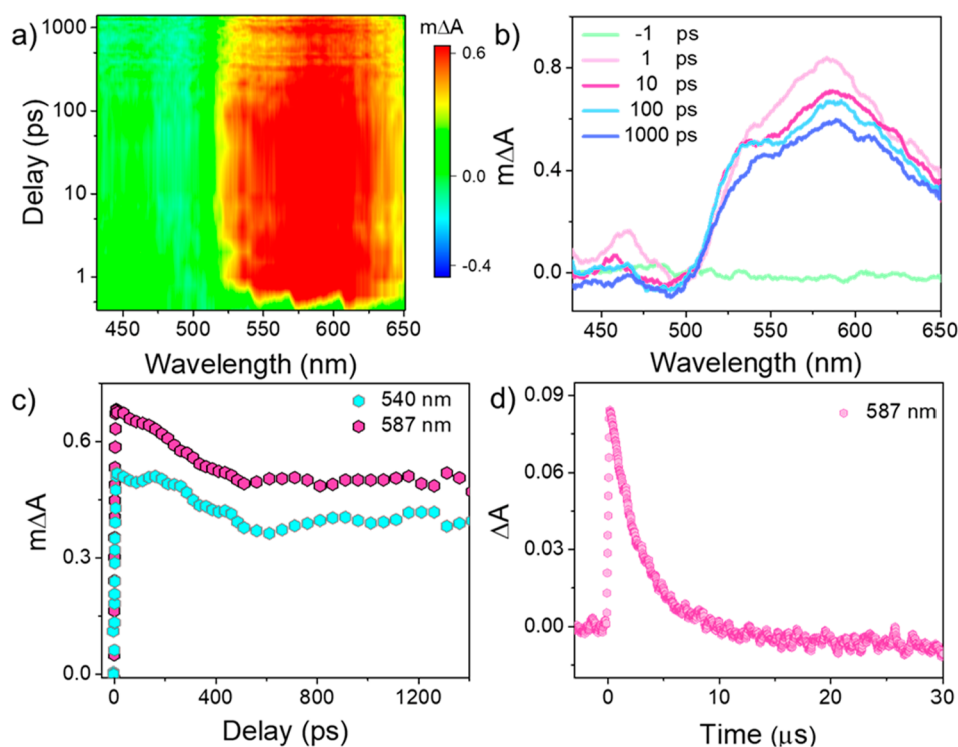


Figure 8. (a) Contour plot of the fs-TA spectrum of Ag_{21} showing broad ESA features from the 520–650 nm region. (b) Time evolution of the spectral profile of ESA features. (c) Femtosecond-decay spectra of ESA indicating higher stability of the excited-state carriers. (d) Nanosecond time evolution spectrum measured using nanosecond laser flash photolysis.

ASSOCIATED CONTENT

Supporting Information

The Supporting Information is available free of charge at <https://pubs.acs.org/doi/10.1021/acs.inorgchem.2c00186>.

Experimental section, instrumentation, theoretical calculations, UV–vis, ESI-MS, CD, FESEM, EDS, PXRD, TEM, XPS, NMR, Fourier transform infrared, HOMO–LUMO, DSC, and associated figures (PDF)

Accession Codes

CCDC 2094436 contains the supplementary crystallographic data for this paper. These data can be obtained free of charge via www.ccdc.cam.ac.uk/data_request/cif, or by emailing data_request@ccdc.cam.ac.uk, or by contacting The Cambridge Crystallographic Data Centre, 12 Union Road, Cambridge CB2 1EZ, UK; fax: +44 1223 336033.

AUTHOR INFORMATION

Corresponding Authors

Thalappil Pradeep – Department of Science and Technology (DST) Unit of Nanoscience and Thematic Unit of Excellence, Department of Chemistry, Indian Institute of Technology (IIT) Madras, Chennai 600036, India; orcid.org/0000-0003-3174-534X; Email: pradeep.iitm.ac.in

Tomas Base – Department of Synthesis, Institute of Inorganic Chemistry, The Czech Academy of Science, Rez 25068, Czech Republic; orcid.org/0000-0003-2533-8705; Email: tbase@iic.acs.cz

Kumaran Nair Valsala Devi Adarsh – Department of Physics, Indian Institute of Science Education and Research Bhopal, Bhopal 462066, India; orcid.org/0000-0002-6337-6545; Email: adarsh@iiserb.ac.in

Authors

Arijit Jana – Department of Science and Technology (DST) Unit of Nanoscience and Thematic Unit of Excellence, Department of Chemistry, Indian Institute of Technology (IIT) Madras, Chennai 600036, India

Parvathy M. Unnikrishnan – Department of Science and Technology (DST) Unit of Nanoscience and Thematic Unit of Excellence, Department of Chemistry, Indian Institute of Technology (IIT) Madras, Chennai 600036, India

Ajay K. Poonia – Department of Physics, Indian Institute of Science Education and Research Bhopal, Bhopal 462066, India; orcid.org/0000-0002-5551-7299

Jayoti Roy – Department of Science and Technology (DST) Unit of Nanoscience and Thematic Unit of Excellence, Department of Chemistry, Indian Institute of Technology (IIT) Madras, Chennai 600036, India

Madhuri Jash – Department of Science and Technology (DST) Unit of Nanoscience and Thematic Unit of Excellence, Department of Chemistry, Indian Institute of Technology (IIT) Madras, Chennai 600036, India

Ganesan Paramasivam – Department of Science and Technology (DST) Unit of Nanoscience and Thematic Unit of Excellence, Department of Chemistry, Indian Institute of Technology (IIT) Madras, Chennai 600036, India

Jan Machacek – Department of Synthesis, Institute of Inorganic Chemistry, The Czech Academy of Science, Rez 25068, Czech Republic; orcid.org/0000-0003-4723-0789

Complete contact information is available at:

<https://pubs.acs.org/doi/10.1021/acs.inorgchem.2c00186>

Notes

The authors declare no competing financial interest.

ACKNOWLEDGMENTS

The authors acknowledge DST, Government of India, and the Ministry of Education, Youth and Sports of Czech Republic for financial support to the bilateral research projects DST/INT/Czech/P-16/2020 and LTAIN19152, respectively. K.N.V.D.A. gratefully acknowledges the Science and Engineering Research Board for Grant CRG/2019/002808. We thank Sophisticated Analytical Instruments Facility, IIT Madras, for the SC-XRD measurements. We thank Sudhadevi Antharjanam and Sujana Manna for SC-XRD and Raman studies, respectively. A.J. thanks IIT Madras for his research fellowship. T.P. acknowledges funding from the Centre of Excellence on Molecular Materials and Functions under the Institution of Eminence scheme of IIT Madras. This work is part of an India–Czech Republic collaboration aimed at exploring the potential of atomically precise nanomaterials produced by combining metal and boron clusters, initiated by T.P. and T.B.

REFERENCES

- (1) Jin, R.; Zeng, C.; Zhou, M.; Chen, Y. Atomically Precise Colloidal Metal Nanoclusters and Nanoparticles: Fundamentals and Opportunities. *Chem. Rev.* **2016**, *116*, 10346–10413.
- (2) Chakraborty, I.; Pradeep, T. Atomically Precise Clusters of Noble Metals: Emerging Link between Atoms and Nanoparticles. *Chem. Rev.* **2017**, *117*, 8208–8271.
- (3) Alhilaly, M. J.; Bootharaju, M. S.; Joshi, C. P.; Besong, T. M.; Emwas, A. H.; Juarez-Mosqueda, R.; Kaappa, S.; Malola, S.; Adil, K.; Shkurenko, A.; Häkkinen, H.; Eddaoudi, M.; Bakr, O. M. $[\text{Ag}_{67}(\text{SPhMe}_2)_{32}(\text{PPh}_3)_8]^{3+}$: Synthesis, Total Structure, and Optical Properties of a Large Box-Shaped Silver Nanocluster. *J. Am. Chem. Soc.* **2016**, *138*, 14727–14732.
- (4) Jana, A.; Chakraborty, P.; Dar, W. A.; Chandra, S.; Khatun, E.; Kannan, M. P.; Ras, R. H. A.; Pradeep, T. Dual Emitting Ag_{35} nanocluster Protected by 2-Pyrene Imine Thiol. *Chem. Commun.* **2020**, *56*, 12550–12553.
- (5) Bootharaju, M. S.; Dey, R.; Gevers, L. E.; Hedhili, M. N.; Basset, J. M.; Bakr, O. M. A New Class of Atomically Precise, Hydride-Rich Silver Nanoclusters Co-Protected by Phosphines. *J. Am. Chem. Soc.* **2016**, *138*, 13770–13773.
- (6) Guan, Z. J.; Zeng, J. L.; Nan, Z. A.; Wan, X. K.; Lin, Y. M.; Wang, Q. M. Thiacalix[4]Arene: New Protection for Metal Nanoclusters. *Sci. Adv.* **2016**, *2*, 1–8.
- (7) Lei, Z.; Wan, X.-K.; Yuan, S.-F.; Guan, Z.-J.; Wang, Q.-M. Alkynyl Approach toward the Protection of Metal Nanoclusters. *Acc. Chem. Res.* **2018**, *51* (10), 2465–2474.
- (8) Liu, K. G.; Hu, M. L.; Jiang, D. E.; Gao, X. M.; Liu, T. All-Carboxylate-Protected Superatomic Silver Nanocluster with an Unprecedented Rhombohedral Ag_8 Core. *J. Am. Chem. Soc.* **2020**, *142*, 16905–16909.
- (9) Cerretani, C.; Kanazawa, H.; Vosch, T.; Kondo, J. Crystal Structure of a NIR-Emitting DNA-Stabilized Ag_{16} Nanocluster. *Angew. Chemie - Int. Ed.* **2019**, *58*, 17153–17157.
- (10) Liu, J. W.; Wang, Z.; Chai, Y. M.; Kurmoo, M.; Zhao, Q. Q.; Wang, X. P.; Tung, C. H.; Sun, D. Core Modulation of 70-Nuclei Core-Shell Silver Nanoclusters. *Angew. Chemie - Int. Ed.* **2019**, *58*, 6276–6279.
- (11) Wang, Z.; Su, H. F.; Kurmoo, M.; Tung, C. H.; Sun, D.; Zheng, L. S. Trapping an Octahedral Ag_6 Kernel in a Seven-Fold Symmetric Ag_{56} Nanowheel. *Nat. Commun.* **2018**, *9* (1), 1–8.
- (12) Diez, I.; Pusa, M.; Kulmala, S.; Jiang, H.; Walther, A.; Goldmann, A. S.; Müller, A. H. E.; Ikkala, O.; Ras, R. H. A. Color Tunability and Electrochemiluminescence of Silver Nanoclusters. *Angew. Chemie - Int. Ed.* **2009**, *48*, 2122–2125.
- (13) Fan, C.; Lv, X.; Liu, F.; Feng, L.; Liu, M.; Cai, Y.; Liu, H.; Wang, J.; Yang, Y.; Wang, H. Silver Nanoclusters Encapsulated into Metal-Organic Frameworks with Enhanced Fluorescence and Specific Ion Accumulation toward the Microdot Array-Based Fluorimetric Analysis of Copper in Blood. *ACS Sensors* **2018**, *3*, 441–450.
- (14) Jin, R.; Li, G.; Sharma, S.; Li, Y.; Du, X. Toward Active-Site Tailoring in Heterogeneous Catalysis by Atomically Precise Metal Nanoclusters with Crystallographic Structures. *Chem. Rev.* **2021**, *121* (2), 567–648.
- (15) Luo, Z.; Zheng, K.; Xie, J. Engineering Ultrasmall Water-Soluble Gold and Silver Nanoclusters for Biomedical Applications. *Chem. Commun.* **2014**, *50*, 5143–5155.
- (16) Han, Z.; Dong, X.; Luo, P.; Li, S.; Wang, Z.; Zang, S.; Mak, T. C. W. Ultrastable Atomically Precise Chiral Silver Clusters with More than 95% Quantum Efficiency. *Sci. Adv.* **2020**, *6* (6), 1–8.
- (17) Yang, H.; Lei, J.; Wu, B.; Wang, Y.; Zhou, M.; Xia, A.; Zheng, L.; Zheng, N. Crystal Structure of a Luminescent Thiolated Ag Nanocluster with an Octahedral Ag_6^{4+} Core. *Chem. Commun.* **2013**, *49*, 300–302.
- (18) Khatun, E.; Bodiuzzaman, M.; Sugi, K. S.; Chakraborty, P.; Paramasivam, G.; Dar, W. A.; Ahuja, T.; Antharjanam, S.; Pradeep, T. Confining an Ag_{10} Core in an Ag_{12} Shell: A Four-Electron Superatom with Enhanced Photoluminescence upon Crystallization. *ACS Nano* **2019**, *13* (5), 5753–5759.
- (19) Joshi, C. P.; Bootharaju, M. S.; Alhilaly, M. J.; Bakr, O. M. $[\text{Ag}_{25}(\text{SR})_{18}]^-$: The “Golden” Silver Nanoparticle. *J. Am. Chem. Soc.* **2015**, *137*, 11578–11581.
- (20) AbdulHalim, L. G.; Bootharaju, M. S.; Tang, Q.; Del Gobbo, S.; AbdulHalim, R. G.; Eddaoudi, M.; Jiang, D. E.; Bakr, O. M. $\text{Ag}_{29}(\text{BDT})_{12}(\text{TPP})_4$: A Tetravalent Nanocluster. *J. Am. Chem. Soc.* **2015**, *137*, 11970–11975.
- (21) Desireddy, A.; Conn, B. E.; Guo, J.; Yoon, B.; Barnett, R. N.; Monahan, B. M.; Kirschbaum, K.; Griffith, W. P.; Whetten, R. L.; Landman, U.; Bigioni, T. P. Ultrastable Silver Nanoparticles. *Nature* **2013**, *501*, 399–402.
- (22) Song, Y.; Lambright, K.; Zhou, M.; Kirschbaum, K.; Xiang, J.; Xia, A.; Zhu, M.; Jin, R. Large-Scale Synthesis, Crystal Structure, and Optical Properties of the $\text{Ag}_{146}\text{Br}_2(\text{SR})_{80}$ Nanocluster. *ACS Nano* **2018**, *12* (9), 9318–9325.
- (23) Bodiuzzaman, M.; Ghosh, A.; Sugi, K. S.; Nag, A.; Khatun, E.; et al. Camouflaging Structural Diversity: Co-Crystallization of Two Different Nanoparticles Having Different Cores but the Same Shell. *Angew. Chemie - Int. Ed.* **2019**, *58*, 189–194.
- (24) Dar, W. A.; Bodiuzzaman, M.; Ghosh, D.; Paramasivam, G.; Khatun, E.; Sugi, K. S.; Pradeep, T. Interparticle Reactions between Silver Nanoclusters Leading to Product Cocrystals by Selective Cocrystallization. *ACS Nano* **2019**, *13*, 13365–13373.
- (25) Deng, G.; Teo, B. K.; Zheng, N. Assembly of Chiral Cluster-Based Metal-Organic Frameworks and the Chirality Memory Effect during Their Disassembly. *J. Am. Chem. Soc.* **2021**, *143*, 10214–10220.
- (26) Yao, Q.; Xie, J. Pasteur-like Separation of Silver Nanocluster Racemates by Conglomerate Crystallization. *ACS Cent. Sci.* **2020**, *6*, 1862–1865.
- (27) Zhang, M. M.; Dong, X. Y.; Wang, Z. Y.; Luo, X. M.; Huang, J. H.; Zang, S. Q.; Mak, T. C. W. Alkynyl-Stabilized Superatomic Silver Clusters Showing Circularly Polarized Luminescence. *J. Am. Chem. Soc.* **2021**, *143*, 6048–6053.
- (28) Kang, X.; Zhu, M. Tailoring the Photoluminescence of Atomically Precise Nanoclusters. *Chem. Soc. Rev.* **2019**, *48*, 2422–2457.
- (29) Alamer, B. J.; Bootharaju, M. S.; Kozlov, S. M.; Cao, Z.; Shkurenko, A.; Nematulloev, S.; Maity, P.; Mohammed, O. F.; Eddaoudi, M.; Cavallo, L.; Basset, J. M.; Bakr, O. M. $[\text{Ag}_9(1,2\text{-BDT})_6]^{3-}$: How Square-Pyramidal Building Blocks Self-Assemble into the Smallest Silver Nanocluster. *Inorg. Chem.* **2021**, *60*, 4306–4312.
- (30) Das, A.; Li, T.; Nobusada, K.; Zeng, C.; Rosi, N. L.; Jin, R. Nonsuperatomic $[\text{Au}_{23}(\text{SC}_6\text{H}_{11})_{16}]^-$ Nanocluster Featuring Bipyramidal Au_{15} Kernel and Trimeric $\text{Au}_3(\text{SR})_4$ Motif. *J. Am. Chem. Soc.* **2013**, *135*, 18264–18267.

- (31) Zhu, M.; Aikens, C. M.; Hollander, F. J.; Schatz, G. C.; Jin, R. Correlating the Crystal Structure of A Thiol-Protected Au₂₅ Cluster and Optical Properties. *J. Am. Chem. Soc.* **2008**, *130*, 5883–5885.
- (32) Li, Y.; Zhou, M.; Jin, R. Programmable Metal Nanoclusters with Atomic Precision. *Adv. Mater.* **2021**, *33*, 2006591.
- (33) Liu, J. Y.; Alkan, F.; Wang, Z.; Zhang, Z. Y.; Kurmoo, M.; Yan, Z.; Zhao, Q. Q.; Aikens, C. M.; Tung, C. H.; Sun, D. Different Silver Nanoparticles in One Crystal: Ag₂₁₀(¹PrPhS)₇₁(Ph₃P)₅Cl and Ag₂₁₁(¹PrPhS)₇₁(Ph₃P)₆Cl. *Angew. Chemie - Int. Ed.* **2019**, *58*, 195–199.
- (34) Yang, H.; Wang, Y.; Chen, X.; Zhao, X.; Gu, L.; Huang, H.; Yan, J.; Xu, C.; Li, G.; Wu, J.; Edwards, A. J.; Dittrich, B.; Tang, Z.; Wang, D.; Lehtovaara, L.; Häkkinen, H.; Zheng, N. Plasmonic Twinned Silver Nanoparticles with Molecular Precision. *Nat. Commun.* **2016**, *7*, 1–8.
- (35) Ma, M. X.; Ma, X. L.; Liang, G. M.; Shen, X. T.; Ni, Q. L.; Gui, L. C.; Wang, X. J.; Huang, S. Y.; Li, S. M. A Nanocluster [Ag₃₀₇Cl₆₂(SPh'Bu)₁₁₀]: Chloride Intercalation, Specific Electronic State, and Superstability. *J. Am. Chem. Soc.* **2021**, *143*, 13731–13737.
- (36) Kang, X.; Wang, S.; Zhu, M. Observation of a New Type of Aggregation-Induced Emission in Nanoclusters. *Chem. Sci.* **2018**, *9*, 3062–3068.
- (37) Sun, Q.-Q.; Li, Q.; Li, H.-Y.; Zhang, M.-M.; Sun, M.-E.; Li, S.; Quan, Z.; Zang, S.-Q. Thermochromism and Piezochromism of an Atomically Precise High-Nuclearity Silver Sulfide Nanocluster. *Chem. Commun.* **2021**, *57*, 2372–2375.
- (38) Li, Q.; Mosquera, M. A.; Jones, L. O.; Parakh, A.; Chai, J.; Jin, R.; Schatz, G. C.; Gu, X. W. Pressure-Induced Optical Transitions in Metal Nanoclusters. *ACS Nano* **2020**, *14*, 11888–11896.
- (39) Yuan, S. F.; Guan, Z. J.; Liu, W. Di; Wang, Q. M. Solvent-Triggered Reversible Interconversion of All-Nitrogen-Donor-Protected Silver Nanoclusters and Their Responsive Optical Properties. *Nat. Commun.* **2019**, *10*, 1–7.
- (40) Bi, Y.; Wang, Z.; Liu, T.; Sun, D.; Godbert, N.; Li, H.; Hao, J.; Xin, X. Supramolecular Chirality from Hierarchical Self-Assembly of Atomically Precise Silver Nanoclusters Induced by Secondary Metal Coordination. *ACS Nano* **2021**, *15* (10), 15910–15919.
- (41) Jana, A.; Jash, M.; Poonia, A. K.; Paramasivam, G.; Islam, M. R.; Chakraborty, P.; Antharjanam, S.; Machacek, J.; Ghosh, S.; Adarsh, K. N. V. D.; Base, T.; Pradeep, T. Light-Activated Intercluster Conversion of an Atomically Precise Silver Nanocluster. *ACS Nano* **2021**, *15* (10), 15781–15793.
- (42) Baksi, A.; Jash, M.; Bag, S.; Mudedla, S. K.; Bodiuzzaman, M.; Ghosh, D.; Paramasivam, G.; Subramanian, V.; Pradeep, T. Mechanistic Elucidation of the Structure and Reactivity of Bare and Hydride-Protected Ag₁₇⁺ Clusters. *J. Phys. Chem. C* **2019**, *123*, 28494–28501.
- (43) Jash, M.; Methikkalam, R. R. J.; Bodiuzzaman, M.; Paramasivam, G.; Pradeep, T. Reaction between Ag₁₇⁺ and Acetylene Outside the Mass Spectrometer: Dehydrogenation in the Gas Phase. *Chem. Commun.* **2020**, *56*, 15623–15626.
- (44) Bootharaju, M. S.; Burlakov, V. M.; Besong, T. M. D.; Joshi, C. P.; Abdulhalim, L. G.; Black, D. M.; Whetten, R. L.; Goriely, A.; Bakr, O. M. Reversible Size Control of Silver Nanoclusters via Ligand-Exchange. *Chem. Mater.* **2015**, *27*, 4289–4297.
- (45) Krishnadas, K. R.; Baksi, A.; Ghosh, A.; Natarajan, G.; Som, A.; Pradeep, T. Interparticle Reactions: An Emerging Direction in Nanomaterials Chemistry. *Acc. Chem. Res.* **2017**, *50*, 1988–1996.
- (46) Neumaier, M.; Baksi, A.; Weis, P.; Schneider, E. K.; Chakraborty, P.; Hahn, H.; Pradeep, T.; Kappes, M. M. Kinetics of Intercluster Reactions between Atomically Precise Noble Metal Clusters [Ag₂₅(DMBT)₁₈]⁻ and [Au₂₅(PET)₁₈]⁻ in Room Temperature Solutions. *J. Am. Chem. Soc.* **2021**, *143*, 6969–6980.
- (47) Poater, J.; Vinas, C.; Bennour, I.; Escayola, S.; Sola, M.; Teixidor, F. Too Persistent to Give Up: Aromaticity in Boron Clusters Survives Radical Structural Changes. *J. Am. Chem. Soc.* **2020**, *142*, 9396–9407.
- (48) Wang, Z.; Wang, M.; Li, Y.; Luo, P.; Jia, T.; Huang, R.; Zang, S.; Mak, T. C. W. Atomically Precise Site-Specific Tailoring and Directional Assembly of Superatomic Silver Nanoclusters. *J. Am. Chem. Soc.* **2018**, *140*, 1069–1076.
- (49) Li, Y.; Wang, Z.; Ma, X.; Luo, P.; Du, C.; Zang, S. Distinct Photophysical Properties in Atom-Precise Silver and Copper Nanocluster Analogues. *Nanoscale* **2019**, *11*, 5151–5157.
- (50) Huang, J.; Wang, Z.; Zang, S.; Mak, T. C. W. Spontaneous Resolution of Chiral Multi-Thiolate-Protected Ag₃₀ Nanoclusters. *ACS Cent. Sci.* **2020**, *6*, 1971–1976.
- (51) Wang, Q.; Wang, J.; Wang, S.; Wang, Z.; Cao, M.; He, C.; Yang, J.; Zang, S.; Mak, T. C. W. O-Carborane Based and Atomically-Precise Metal Clusters as Hypergolic Materials. *J. Am. Chem. Soc.* **2020**, *142* (28), 12010–12014.
- (52) Dhayal, R. S.; Liao, J. H.; Liu, Y. C.; Chiang, M. H.; Kahlal, S.; Saillard, J. Y.; Liu, C. W. Ag₂₁{S₂P(OⁱPr)₂}₁₂⁺: An Eight-Electron Superatom. *Angew. Chemie - Int. Ed.* **2015**, *54*, 3702–3706.
- (53) Chang, W. T.; Lee, P. Y.; Liao, J. H.; Chakrahari, K. K.; Kahlal, S.; Liu, Y. C.; Chiang, M. H.; Saillard, J. Y.; Liu, C. W. Eight-Electron Silver and Mixed Gold/Silver Nanoclusters Stabilized by Selenium Donor Ligands. *Angew. Chemie - Int. Ed.* **2017**, *56*, 10178–10182.
- (54) Li, Y.; Zhou, M.; Song, Y.; Higaki, T.; Wang, H.; Jin, R. Double-Helical Assembly of Heterodimeric Nanoclusters into Super-crystals. *Nature* **2021**, *594*, 380–384.
- (55) Walter, M.; Akola, J.; Lopez-Acevedo, O.; Jadzinsky, P. D.; Calero, G.; Ackerson, C. J.; Whetten, R. L.; Grönbeck, H.; Häkkinen, H. A Unified View of Ligand-Protected Gold Clusters as Superatom Complexes. *Proc. Natl. Acad. Sci. U. S. A.* **2008**, *105* (27), 9157–9162.
- (56) Weerawardene, K. L. D. M.; Häkkinen, H.; Aikens, C. M. Connections between Theory and Experiment for Gold and Silver Nanoclusters. *Annu. Rev. Phys. Chem.* **2018**, *69*, 205–229.
- (57) Goebbert, D. J.; Garand, E.; Wende, T.; Bergmann, R.; Meijer, G.; Asmis, K. R.; Neumark, D. M. Infrared Spectroscopy of the Microhydrated Nitrate Ions NO₃(H₂O). *J. Phys. Chem. A* **2009**, *113*, 7584–7592.
- (58) Leites, L. A. Vibrational Spectroscopy of Carboranes and Parent Boranes and Its Capabilities in Carborane Chemistry. *Chem. Rev.* **1992**, *92* (2), 279–323.
- (59) Sugi, K. S.; Bandyopadhyay, P.; Bodiuzzaman, M.; Nag, A.; Hridaya, M.; Dar, W. A.; Ghosh, P.; Pradeep, T. Manifestation of Structural Differences of Atomically Precise Cluster-Assembled Solids in Their Mechanical Properties. *Chem. Mater.* **2020**, *32*, 7973–7984.
- (60) Lin, X.; Cong, H.; Sun, K.; Fu, X.; Kang, W.; Wang, X.; Jin, S.; Wu, R.; Liu, C.; Huang, J. One-Step Rapid Synthesis, Crystal Structure and 3.3 Microseconds Long Excited-State Lifetime of Pd₁Ag₂₈ Nanocluster. *Nano Res.* **2020**, *13* (2), 366–372.